

Cluster Curlometry Limitations in the Ring Current Region

T. B. Keebler¹, M. W. Liemohn¹, N. Y. Ganushkina^{1,2}

¹ Department of Climate and Space Sciences and Engineering, University of Michigan, Ann Arbor, MI.

² Space Research and Observation Technologies, Space and Earth Observation Centre, Finnish Meteorological Institute, Helsinki, Finland

Corresponding author: Timothy Keebler (tkeebler@umich.edu)

In preparation for/Submitted to *Journal of Geophysical Research Space Physics*

Key Points:

- Examination of Cluster curlometer output shows strong evidence of contamination by linearization errors in the ring current region.
- False currents are computed by the curlometer when a large tetrahedron dimension aligns with the magnetic gradient.
- The curlometer technique has highly constrained utility in the inner magnetosphere that requires careful consideration of limitations.

AGU Index Terms:

- 2730 Magnetosphere: inner
- 2778 Ring current
- 2794 Instruments and techniques
- 7833 Mathematical and numerical techniques (0500, 3200)

Keywords:

Ring Current, Cluster II, Curlometer

24 **Abstract**

25 During its ongoing mission, the Cluster II constellation has provided the first small-scale
26 multipoint measurements of the space environment, and dramatically advanced scientific
27 understanding in numerous regimes. One such region is the Earth's inner magnetospheric ring
28 current, which could now be computed using the curl of the magnetic field over a spacecraft
29 tetrahedron instead of via plasma moments. While this produced the first 3D current estimates, it
30 also produced different results from prior ring current studies with differing magnitudes and
31 correlations with storm indices/local times. In this analysis, we revisit Cluster ring current data via
32 curlometry, and conduct additional quantitative sensitivity simulations using actual spacecraft
33 position data. During the orbits that observed ring current structure, tetrahedron shape and linearity
34 assumptions can create large errors up to 100% of physical current magnitude in curlometer output
35 that contradict accepted estimated quality parameters. These false currents are directly related to
36 the structure of the current environment, and cannot be distinguished from the actual currents
37 without additional limiting assumptions. The trustworthiness of curlometer output in the ring
38 current is therefore dependent on the linearity of the magnetic structure relative to the tetrahedron
39 orientation, which requires additional characterization. The Cluster curlometer output in the ring
40 current is then explored in light of these new uncertainties, with the computed current magnitude
41 and direction both potentially impacted by the production of false currents.

42 **Plain Language Summary**

43 The ring current is a structure in near-Earth space that causes magnetic changes on the
44 Earth's surface and is very important for plasma transport as well. Previously, it has been measured
45 using single spacecraft by sampling the electrically charged particles. However, the Cluster
46 mission allowed the ring current to be calculated in greater detail by observing magnetic fields,
47 which are easier to measure. This technique was dubbed the 'curlometer,' and has applications in
48 many regions. For the ring current region in particular, the curlometer technique produces very
49 different ring current strengths than the particle-measurement methods. To resolve this, we
50 reevaluated the curlometer technique and tested it against simulated data for which the current can
51 be analytically calculated, showing larger uncertainty than previously thought. Thus, the
52 curlometer has limitations for using the Cluster mission to measure the ring current.

53 **1. Introduction**

54 The Cluster II multi-spacecraft mission, launched in 2000, has been a resounding success
55 in probing a multitude of environments by collecting data in varying three-dimensional
56 configurations. By providing multipoint measurements, Cluster benefits from improved
57 calibration and novel techniques that cannot be implemented by a single spacecraft (Paschmann &
58 Daly, 2000). One such technique has been named the ‘curlometer,’ because it uses the four
59 spacecraft as vertices of a tetrahedron to compute the linearized gradient of magnetic field and find
60 the average current density in the tetrahedron volume (Dunlop et al., 1988). Although requiring
61 limitations and assumptions, the curlometer technique has been applied to many regions containing
62 magnetic structure that has a larger characteristic scale than the tetrahedron (Dunlop et al., 2016).
63 Thus, we have gained additional insight into the three-dimensional current structure of features
64 from the cusp to the magnetotail (e.g., Henderson et al., 2008; Dunlop et al., 2015; Petrukovich et
65 al., 2014).

66 In the ring current region of the inner magnetosphere ($\sim 3\text{-}7 R_E$) (e.g., see reviews and
67 references by Ganushkina et al., 2018, and Dandouras et al., 2018), the curlometer technique has
68 been applied to provide a better estimate of ring current magnitudes critical for understanding
69 storm indices and current closure, also qualitatively capturing field-aligned currents in this region
70 (Vallat et al., 2005; Zhang et al., 2011). Curlometry offers an alternative to computing current from
71 plasma pressure moments, which have higher uncertainty through methodology and
72 instrumentation (Dandouras & Barthe, 2011). Pressure moments can also only yield a single
73 component of current orthogonal to the plane defined by the spacecraft trajectory and local
74 magnetic field, whereas curlometry provides the full current vector.

75 Currents computed from Cluster via curlometry in the ring current region suggest a
76 westward current that varies from near zero to a few tens of nA/m^2 . Vallat et al. (2005) found that
77 the magnitude had no correlation with geomagnetic activity indicated by the Disturbance Storm
78 Time (Dst) index (see Figure 16 and Section 7, Vallat et al., 2005), and using subsequent orbits,
79 other papers (Zhang et al., 2011; Grimald et al., 2012; Shen et al., 2014) have built statistical
80 compilations for the ring current using different thresholds for storm/quiet delineation. However,
81 these results are contrary to plasma moment and single spacecraft magnetometer current
82 calculations, which suggest currents approaching 10 nA/m^2 occur only near storm-times, and are

83 consistently weaker than this value with lower activity (e.g., Lui et al., 1992; Greenspan &
 84 Hamilton, 2000; Jorgensen et al., 2004; Le et al., 2004). Furthermore, time series or radial plots of
 85 curlometer output (i.e., Vallat et al., 2005) often show structure that is inconsistent with
 86 expectations; namely, near-constant current magnitude instead of an inverse relation with L-shell
 87 (assuming the pressure peak is radially inward of perigee). These discrepancies urge a thorough
 88 reanalysis of Cluster data to account for these observational differences and to probe the underlying
 89 assumptions of current calculation (Liemohn et al., 2016). Herein, an approach to curlometry that
 90 is mindful of limitations caused by tetrahedron geometry and alignment is developed to
 91 characterize the curlometer technique’s ability to reproduce known current systems. We assess the
 92 Cluster tetrahedron configurations near perigee relative to imposed idealized current sheets,
 93 examining the resulting current densities obtained from linear curlometry calculations. Through
 94 simulation, the conditions that cause the curlometer to produce false currents are quantitatively
 95 characterized, adding a better understanding of the uncertainties associated with these ring current
 96 measurements. Through simulation, the conditions that cause the curlometer to produce false
 97 currents are quantitatively characterized, adding a better understanding of the uncertainties
 98 associated with these ring current measurements.

99 **2. Methodology**

100 **2.1. Implementation of the Curlometer Technique**

101 The curlometer technique has been well-documented in numerous papers (e.g., Dunlop et
 102 al., 1988; Robert et al., 1998; Vallat et al., 2005); thus, only a brief discussion is provided here.
 103 According to the Maxwell-Ampere Law, and assuming stationarity (removal of time dependence
 104 term):

$$105 \quad \mu_0 \vec{J} = \nabla \times \vec{B} \quad (1)$$

106 which can be rewritten with respect to a reference magnetic field vector at a reference location:

$$107 \quad \vec{J} \cdot \left((\vec{r}_i - \vec{r}_{ref}) \times (\vec{r}_j - \vec{r}_{ref}) \right) = \frac{1}{\mu_0} \left((\vec{B}_i - \vec{B}_{ref}) \cdot (\vec{r}_j - \vec{r}_{ref}) - (\vec{B}_j - \vec{B}_{ref}) \cdot (\vec{r}_i - \vec{r}_{ref}) \right) \quad (2)$$

108 With four spacecraft, the curl of the magnetic field can be computed by cyclically differencing
 109 over each face of the tetrahedron to find the three-dimensional linear gradients and summing
 110 (Equation 2), yielding the average current density within the tetrahedron volume. Note that in

111 Equation 2, 'r' denotes the spacecraft position vector, the 'ref' subscript refers to the reference
112 spacecraft, and the 'i' and 'j' subscripts are iterated through non-reference spacecraft pairs. A more
113 detailed treatment of the technique can be found in Dunlop et al. (1988) or Middleton and Masson
114 (2016).

115 For this study, the curlometer computation was performed by modifying a Python script
116 provided by the Cluster Science Archive (CSA) ([http://www.cosmos.esa.int/web/csa/multi-](http://www.cosmos.esa.int/web/csa/multi-spacecraft/)
117 [spacecraft/](http://www.cosmos.esa.int/web/csa/multi-spacecraft/)). The script was thoroughly tested for correct methodology: first with sample data
118 provided by CSA, then by alternating reference spacecraft and perturbing parameters, and finally
119 by 'flying' the constellation through simulated linear current environments. In each case, the
120 output was as expected, demonstrating independence of reference spacecraft choice and correctly
121 capturing the simulated currents. This analysis followed the work of Robert et al. (1998) and
122 independently confirmed the results of that study. The code was further verified by replacing
123 magnetic field data with constant field, correctly producing no current, with an idealized dipole
124 field, producing small current ($< 2 \text{ nA/m}^2$) due to nonlinear magnetic gradients, and with the
125 International Geomagnetic Reference Field (IGRF) (Alken et al., 2021), which also created only
126 small current outputs ($< 3 \text{ nA/m}^2$ with 2002 tetrahedra) as expected (Dunlop et al., 2020). Thus,
127 the curlometer script was confirmed to function correctly in a variety of environments. A sample
128 of these tests for different tetrahedra is provided in supplemental material. Extensive testing
129 provided the necessary foundation for later conclusions by definitively verifying the curlometer
130 computation.

131 Magnetic field data from the Fluxgate Magnetometer (FGM) instruments on each
132 spacecraft were obtained in spin resolution along with spacecraft ephemeris data. The resolution
133 of the magnetometer measurement at the observed field strength is roughly 0.125 nT (Balogh et
134 al., 1997); the effect of this resolution was determined to be no more than $\pm 2 \text{ nA/m}^2$ in curlometer
135 output in agreement with the analysis done by Vallat et al. (2005), and a sample is provided in
136 supplemental material. For this present study, temporal data resolution was experimentally
137 determined to have only a small effect on current values, within the ranges of available datasets;
138 therefore, spin resolution ($\sim 4 \text{ s}$ cadence) sufficiently captures the scale of desired features. All
139 values were converted from Geocentric Solar Ecliptic (GSE) to Solar Magnetic (SM) coordinates
140 using the SpacePy Python package (Morley et al., 2011) and tested to ensure they retained their
141 magnitudes. Note that westward azimuthal current is defined to be positive due to convention in

142 prior studies. IGRF values were then subtracted from the magnetic field data to remove as much
143 nonlinear magnetic gradient as possible and therefore allow a more robust linearity assumption
144 and curlometry result (Dunlop et al., 2016; Dunlop et al., 2020). This has a significant effect on
145 current densities for spacecraft separations above 200 km.

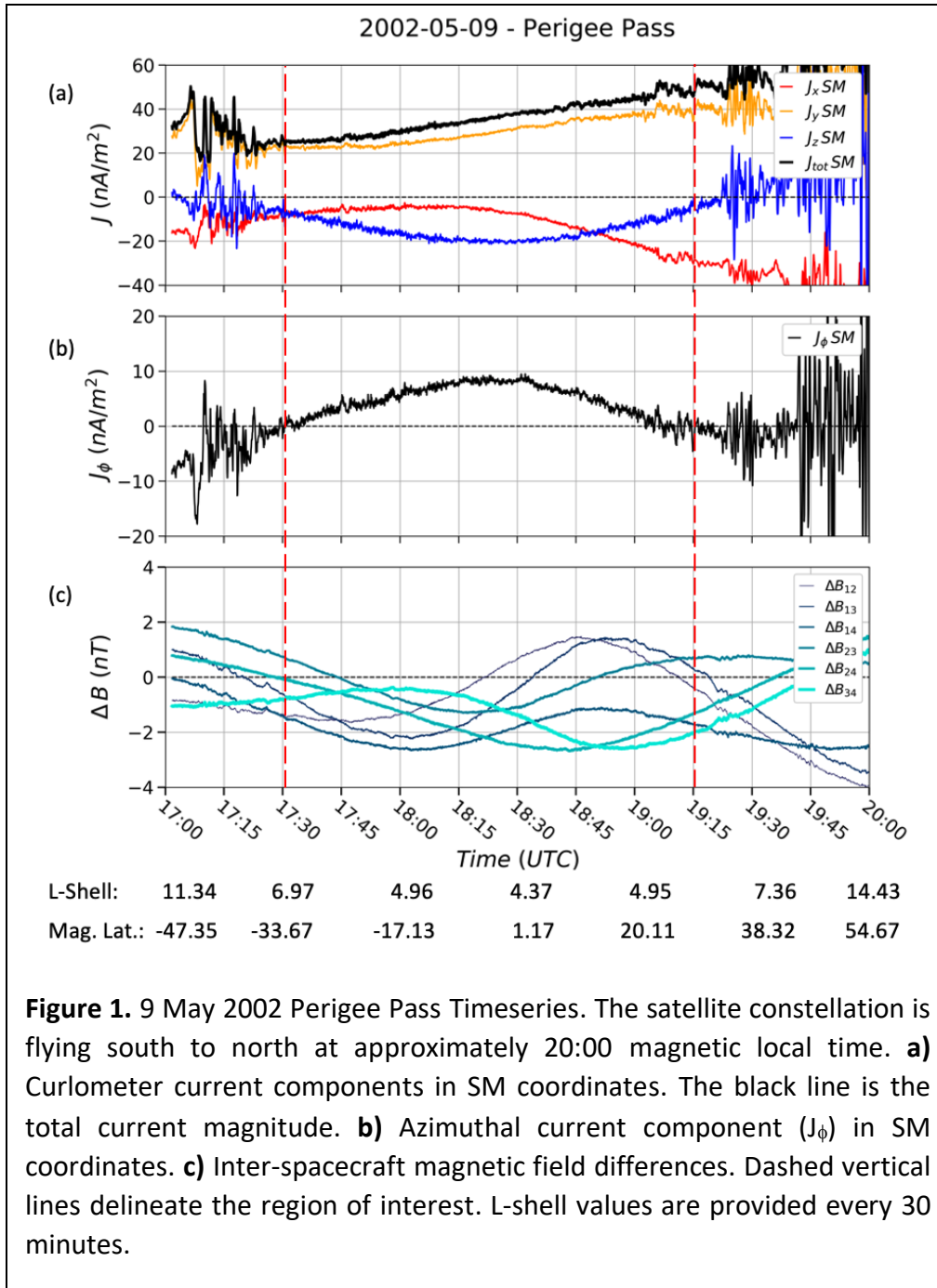
146 **2.2. Ring Current Event Selection**

147 During the period of study for this analysis, the Cluster spacecraft operated in highly-
148 elliptical orbits with perigee of $\sim 4 R_E$, apogee of $\sim 20 R_E$, inclination of $\sim 90^\circ$, and period of ~ 57
149 hours. The spacecraft flew in various evolving formations that had interspacecraft separations less
150 than 1000 km. The Cluster tetrahedron was most regular within the ring current region for select
151 dates from 2001-2004, which is critical for accurate curlometer output. Using prior studies for
152 guidance in event selection (Vallat et al., 2005; Zhang et al., 2011; Shen et al., 2014), six hours of
153 data surrounding every perigee pass individually underwent visual inspection. Each pass was run
154 through the curlometer script and examined. Perigee passes were removed if data was missing
155 from anywhere in the expected ring current region, or if there were obvious errors in the data (e.g.,
156 discontinuities, asymptotes). This filtering of missing data therefore removed passes that
157 experienced eclipses.

158 Figure 1 presents an example of the Cluster data examined for this study, specifically from
159 the 9 May 2002 perigee pass, when the tetrahedron shape was within the nominal guidelines for
160 yielding reasonable current densities from the curlometer technique. The tetrahedron characteristic
161 size was just under 200 kilometers, with the largest separation at about 250 kilometers. This pass
162 has a minimum radial distance of $4.3 R_E$ and a magnetic local time near 20:00. The timeseries
163 shown is from south to north, maintaining the magnetic local time near 20:00 with only small
164 deviations from meridional motion. The magnetic equator is at approximately 18:20 UTC, with
165 Southern Hemisphere observations prior to that time and Northern Hemisphere observations
166 subsequently. The top two panels show the current density computed from the curlometer Python
167 script, first in SM coordinates (Figure 1a) and then just the azimuthal component (Figure 1b). In
168 Figure 1a, the total current magnitude is plotted in the black line, while colored lines are Cartesian
169 current components. Figure 1c shows the interspacecraft differences in magnetic field magnitude
170 used in the curlometer calculation. Spacecraft geometric parameters, tetrahedron quality, and

171 radial current are also plotted for reference in the supplemental material. The vertical red dashed
172 lines roughly outline the region of interest, as marked by smooth curlometer output.

173 Several features are readily seen in Figure 1. First, there is a smooth section of current
174 around the magnetic equator, surrounded by intervals with highly fluctuating currents. Second, the
175 magnetic field differences do not show a drastic change at the variable/smooth boundary (the red-
176 dashed vertical lines). That is, the current densities come from rather small deviations in magnetic
177 field differences, sometimes hardly noticeable on the plotted scales. The perturbations in the
178 magnetic field that cause large oscillations in the current are very small, less than 0.1 nT, and the
179 differences across the tetrahedron (Figure 1c) that are used for computing current are far smaller
180 than the typical field strength at this distance of about 400 nT. Also note an apparent symmetry in
181 the azimuthal current along the trajectory, as expected.



182

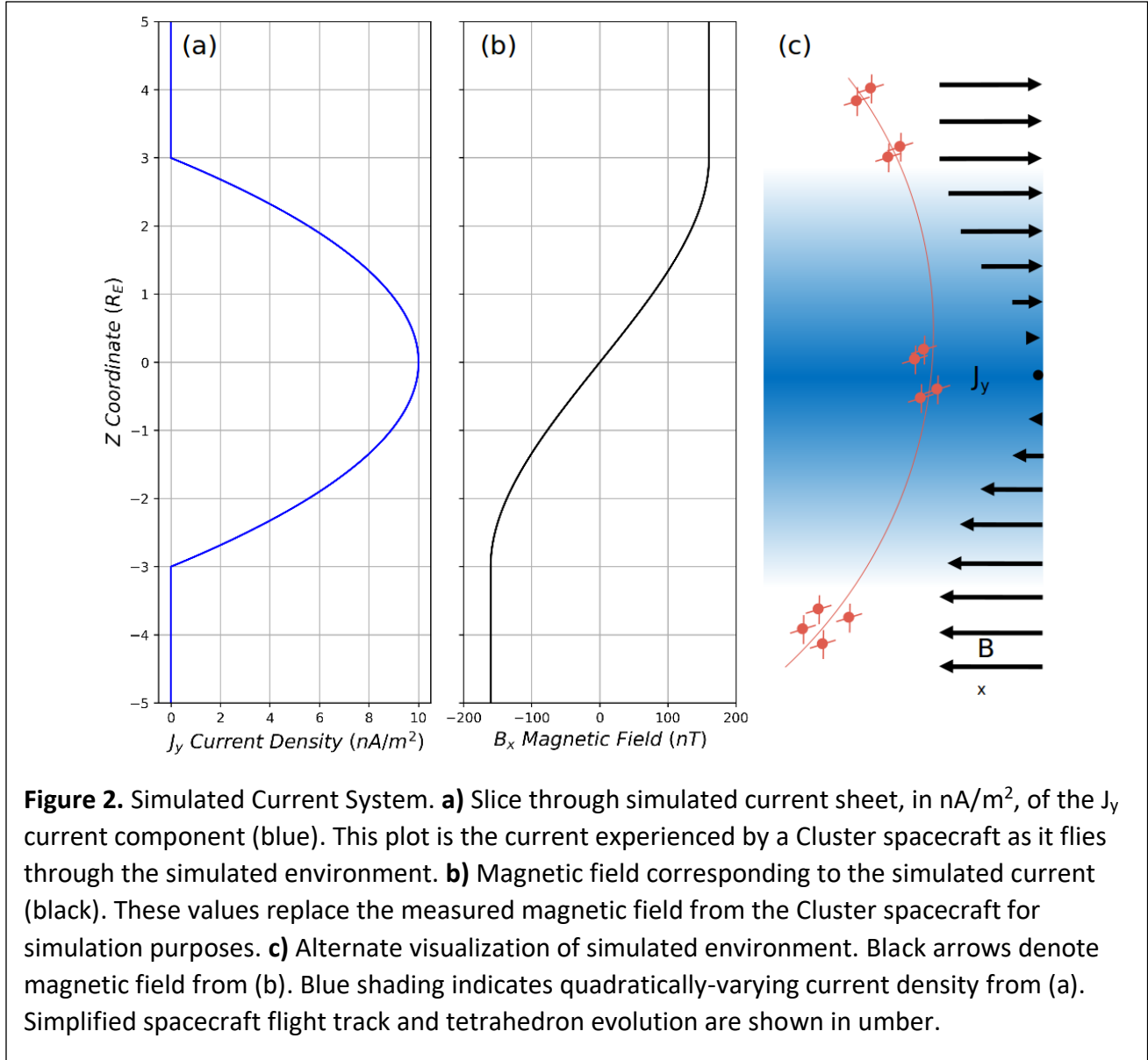
183 Similarly to the example in Figure 1, all perigee passes were examined to capture and
 184 identify the region of interest as the area with smooth current profile. Outside the region of smooth
 185 current signatures (outside red dashed lines), curlometry yields wildly oscillating current
 186 components as a result of the complex structure in these regions below the tetrahedron scale size
 187 (Vallat et al., 2005). Conversely, the presumed ring current section of the orbit is marked by a

188 smooth timeseries indicating a homogeneous structure. After identification, the set of all cases was
189 then used to demonstrate the uncertainties detailed herein.

190 **2.3. Nonlinear Current Simulations and Tetrahedron Shape**

191 To investigate the performance of the curlometer in different environments, simplified
192 simulations were used to probe for possible error. When testing curlometry through simulated
193 magnetic fields, deviation from linear magnetic gradient causes errors in the output current. Robert
194 et al. (1998) suggests that this effect is <10% for a regular tetrahedron with elongation and
195 planarity both below 0.8 (see Paschmann & Daly (1998), Chapter 13, for detailed treatment of
196 tetrahedron geometric parameters). Defined as the ratio between magnetic divergence and
197 magnetic curl, the quality parameter $Q = |\text{div}(\mathbf{B})|/|\text{curl}(\mathbf{B})|$ has also been used to determine regions
198 where the curlometer has better performance, with $Q = 0.5$ as the standard threshold (e.g., Dunlop
199 et al., 1988, Vallat et al., 2005, Zhang et al., 2011). However, a comparison between idealized
200 current as input and curlometer output has not been conducted using actual spacecraft position
201 data. This process is distantly similar to that of Dunlop et. al (2002), but uses a more idealized
202 situation and a more focused region of interest.

203 To represent the simulated currents, an infinite planar current sheet was constructed with
204 thickness scaled to the selected perigee pass and quadratic variation from 0 nA/m² at the
205 boundaries to 10 nA/m² at the center; the simulated current sheet was then offset to the center of
206 the selected spacecraft flight track. Although greatly oversimplified, this model creates gradients
207 consistent with structural understanding of the magnetosphere (eg. Le et al., 2004) and of similar
208 magnitude as proposed by Vallat et al. (2005). Using the Biot-Savart law, the magnetic field
209 vectors were computed at each spacecraft location, then passed through the curlometer script. A
210 simplified visualization is provided in Figure 2, depicting the spacecraft trajectory, variation of
211 current, and magnetic field for a single case. Figure 2a shows the current density constructed for
212 the simulated system in blue; the corresponding magnetic field generated by this current is in
213 Figure 2b in black. Finally, Figure 2c shows another representation of the current density as blue
214 shading, magnetic field as black arrows, and a cartoon Cluster constellation flying through the
215 simulated environment from bottom to top in red.



216

217

218

219

220

221

222

223

Because the Cluster tetrahedron had some degree of irregularity in shape near perigee on all orbits, the simulated current sheets were iterated through all orientations and current directions. In other words, the simulated current sheets were constructed in each component direction, J_x , J_y , and J_z , and also with the current sheet normal direction varied for each case. Additionally, for each current sheet orientation, the tetrahedron was rotated about the barycenter by way of individual spacecraft positions and reanalyzed to deduce the combined effect of current direction and

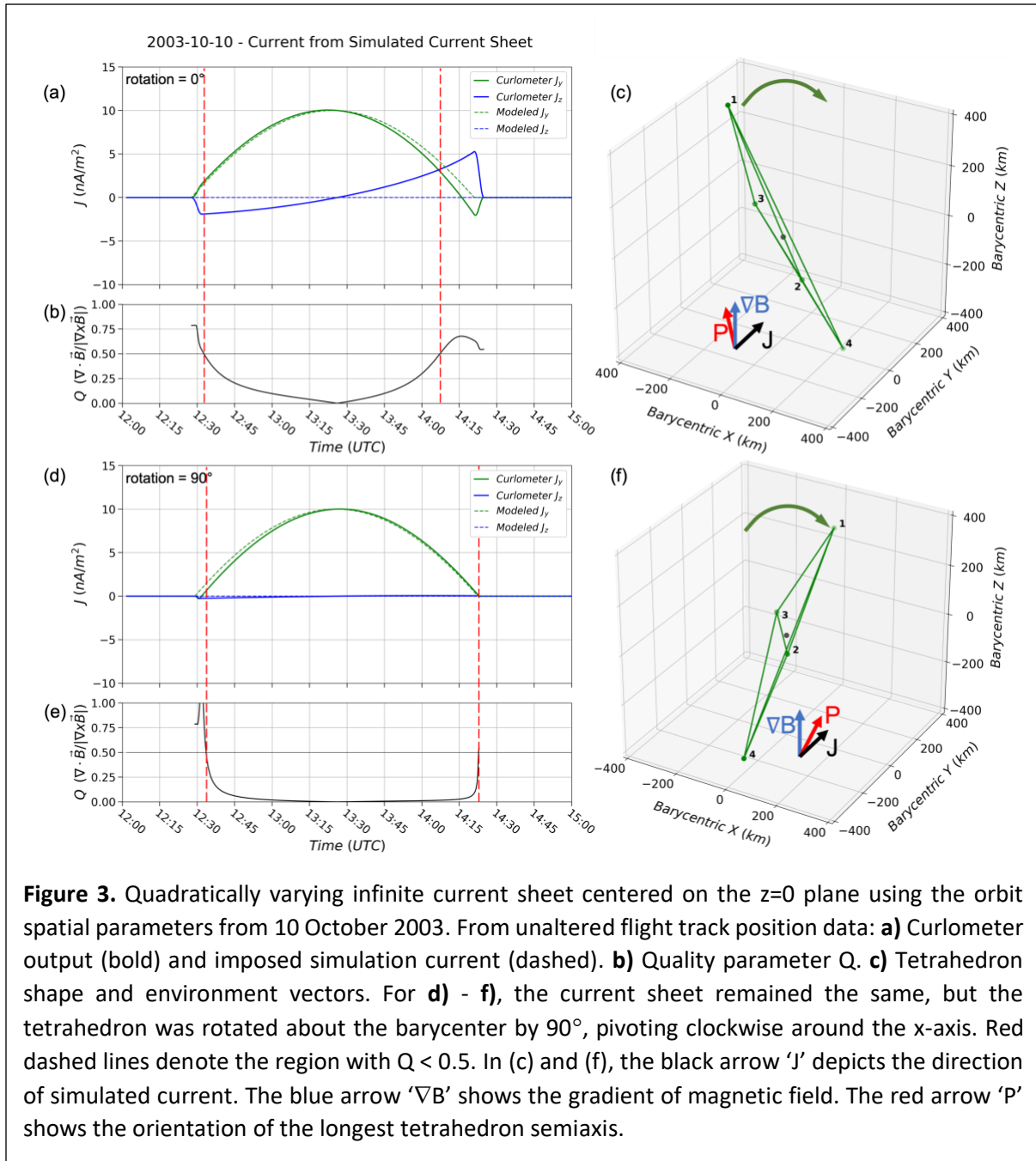
224 tetrahedron aspect. Thus, the possible geometric combinations of the simulated current and
225 tetrahedron were completely explored for the ring current environment as observed by Cluster.

226 **3. Results**

227 As discussed in the methodology section above, idealized current configurations were used
228 to replace the observed Cluster magnetometer data with simulated data, for which the
229 corresponding current density is known. Figure 3 shows the results of an idealized current sheet in
230 the J_y direction centered in the $z = 0$ plane. The current density varies quadratically from $J = 0$ at
231 the boundaries to a maximum in the center of 10 nA/m^2 with a total thickness of $5 R_E$. This
232 thickness was based on the observed ring current thickness of the selected event. The tetrahedron
233 was ‘flown through’ the simulation using actual position data from 10 October 2003 (other events
234 provided in supplemental materials) and replacing the magnetic field with values computed from
235 the simulated current sheet using the Biot-Savart law (Figures 3a-3c). Figure 3a shows the
236 calculated currents from the original unrotated tetrahedron, with the imposed currents represented
237 by dashed lines and the calculated currents represented by solid lines. The green lines are the J_y
238 component, which is the imposed component that is expected to be captured. The blue lines are
239 the J_z component, which is set to 0 in the imposed current and expected to be computed as 0 as
240 well. Figure 3b contains the corresponding quality parameter Q . The boundaries of the threshold
241 $Q = 0.5$ are marked with vertical red dashed lines. In Figure 3c, the locations of all spacecraft
242 relative to the constellation barycenter are plotted as the vertices of the tetrahedron, to visualize
243 the constellation shape. Figure 3c also contains arrows to show relevant vector directions,
244 including current direction (black arrow), magnetic gradient (blue arrow), and longest planar axis
245 (red arrow). Note that the planarity vector shows the direction of the largest semiaxis, instead of
246 the planarity normal direction. The tetrahedron was then rotated about its barycenter around the x -
247 axis by 90° to produce Figures 3d-3f. Figure 3d shows the currents as in Figure 3a, Figure 3e shows
248 the Q calculation as in Figure 3b, and Figure 3f shows the constellation as in Figure 3c, following
249 the 90° rotation.

250 It is immediately apparent that, despite the simulated current being purely in the J_y
251 direction, a large false current is output by the curlometer technique because of the non-zero J_z
252 current. In this instance, the false current grew as large as 5 nA/m^2 in the J_z direction (solid blue
253 line, Figure 3a). The unaltered tetrahedron orientation produced nearly the greatest false currents

254 of any rotation direction. Furthermore, the large false currents occur well below the $Q < 0.5$ quality
255 standard in Figure 3b, with significant stature even at more stringent thresholds. In other words,
256 the false currents occur between the red dashed lines denoting acceptable curlometer quality.
257 Rotating the tetrahedron about its barycenter, however, produced different results (Figure 3d).
258 Instead of a large false current, the same tetrahedron parameters with a quarter rotation captured
259 the currents remarkably well with little deviation between dashed and solid lines (Figure 3d), and
260 Q is much lower throughout the pass (Figure 3e). All else equal, rotation dramatically changed the
261 output by altering the planar direction with respect to the magnetic field gradient. When rotated
262 farther, currents appear again, related to the orientation of magnetic gradient with respect to planar
263 direction. An animation of rotating the tetrahedron with corresponding curlometer output is
264 provided in supplemental materials. Larger false currents are produced when the largest planar
265 semiaxis is more parallel to the magnetic gradient; this can be seen by comparing the red and blue
266 arrows in Figures 3c and 3f. During analysis, the tetrahedron was rotated independently and in
267 combination of all three axes, with only the extrema of false currents highlighted in the figure.
268 Rotation about other axes produced smaller false currents, so the uncertainty contributions from
269 those axes are smaller. False currents are directly related to the length of the tetrahedron semiaxis
270 parallel to the magnetic gradient; therefore, some rotations will roughly preserve that quantity.



271

272

273

274

275

276

277

Using simulated currents and tetrahedron rotations like those that produced Figure 3, the curlometer calculation yielded large non-physical currents in complementary components with different simulated current directions and tetrahedron rotation axes as well. Despite this example emphasizing the production of J_z , gradients in other directions do impact the azimuthal current in the same way. Thus, without a priori knowledge of the environment, false currents may appear in any direction depending on the gradients present. These false currents are in the direction of the

278 magnetic gradient associated with the magnetospheric current sheet (like the spurious J_z in Figure
279 3a), but the magnitude was highly dependent on tetrahedron orientation and shape parameters.
280 Even in regions where $Q < 0.5$ for the curlometer computation, false currents could be as much as
281 100% of the imposed current at a given time (5 nA/m^2 of J_z created by 5 nA/m^2 of J_y), with
282 significant implications that ring current curlometry can be highly inaccurate despite accepted data
283 filtering methods.

284 Rotating the tetrahedron about the barycenter provided additional insight into the
285 relationship between shape, orientation, and false current. Elongation was consistently near 0.8 for
286 all passes and timestamps, but planarity evolved quickly from 0.4 to near unity in the few hours
287 surrounding perigee. Thus, planarity was observed to have the larger effect of the shape parameters
288 in these flight tracks, and maximum false current was produced by the largest planarity semiaxis
289 that was close to being parallel to ∇B and therefore experiencing the largest linearization error. In
290 cases with multiple gradients, false and physical currents added linearly through the curlometer,
291 requiring understanding of physical currents to deduce the false components. However, false
292 current was also strongly related to nonlinearity in magnetic gradient, so without quantitative
293 knowledge of this it is impossible to correct in-situ data for these differences. Numeric correction
294 of curlometer output requires additional study and technique development and will be severely
295 limited by enhanced stationarity assumptions.

296 **4. Application to Cluster Data**

297 Considering the production of false currents in the simulated environment, this section
298 provides an initial view of the Cluster ring current observations in the context of increased
299 uncertainty. The application of the curlometer technique to this dataset produces current structures
300 that are consistent with nonlinearity current artifacts as seen in the simulated currents.

301 **4.1. Representative Curlometry**

302 Previously in this study and others (e.g., Vallat et al., 2005, Zhang et al., 2011), the quantity
303 $Q = \text{div}(\mathbf{B})/\text{curl}(\mathbf{B})$ was used as a quality flag, with values less than 0.5 considered acceptable
304 uncertainty. However, simulated currents can produce false results with the same order of
305 magnitude as the imposed currents even when Q is below the 0.5 threshold (as seen in Figure 3),
306 depending on tetrahedron orientation. Orbits in the Cluster dataset each only contain a small

307 duration under this threshold and are likely to contain larger magnitude errors outside this range.
308 While the latitudinal extent of the ring current can be established with reasonable confidence via
309 plasma data and regularity of current profile, information regarding the magnitude and direction
310 of the current may be grossly inaccurate. Examining tetrahedron orientation through simulated
311 current sheets produced new maximum uncertainty estimates that exceed the elongation-planarity
312 plots constructed by Robert et al. (1998), which suggest current magnitude errors rarely exceed a
313 mere 10% when both elongation and planarity are below 0.8 (see, for example, Figures 16.7 and
314 16.8 in Robert et al., 1998).

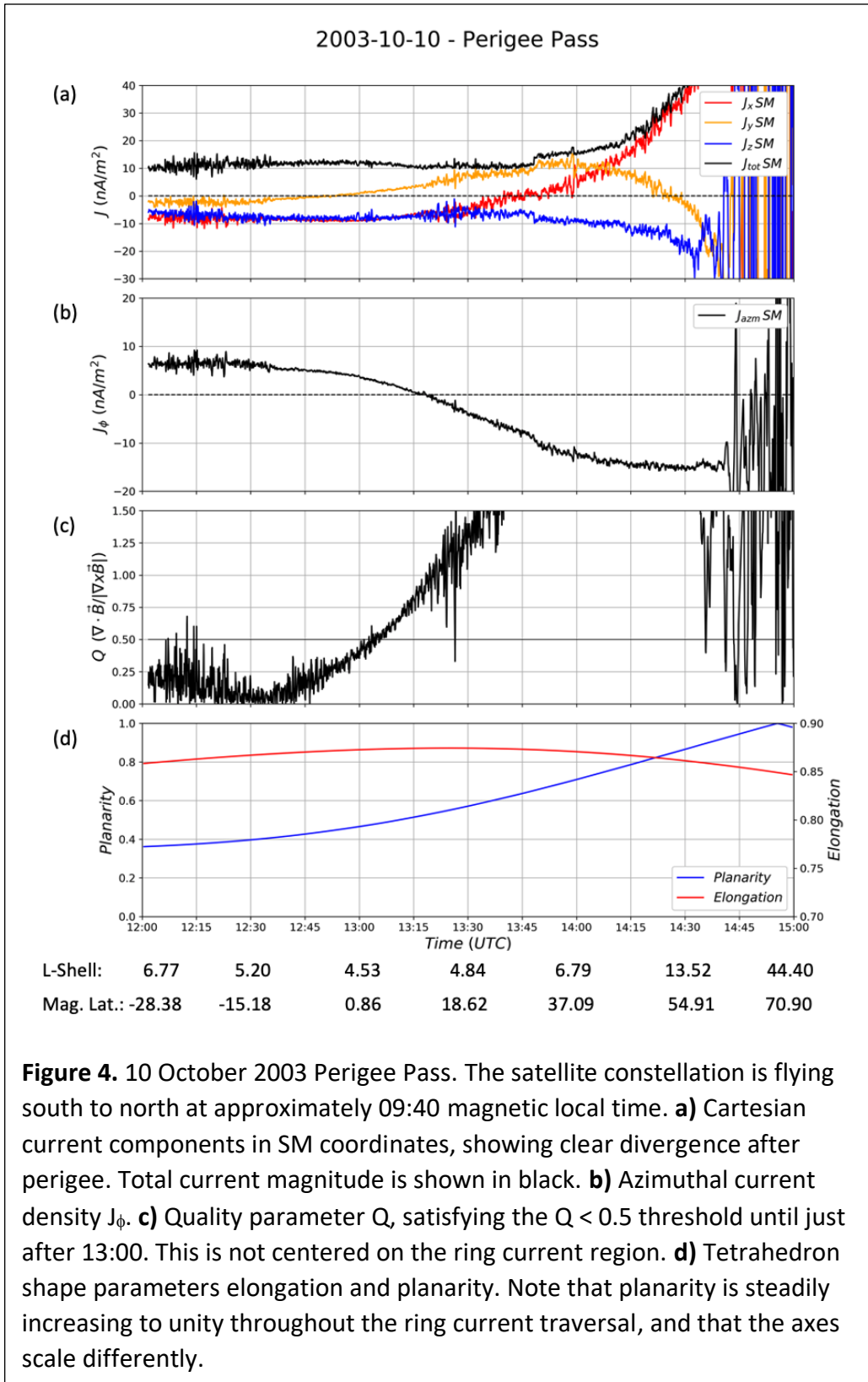
315 New selection criteria for suitable ring current data must examine the curlometer output in
316 conjunction with the quality parameter Q and a priori knowledge of the magnetospheric
317 environment to judge data validity. Only data with a maximum Q of 0.5 should be considered in
318 climatological studies of the ring current because instances above this threshold almost certainly
319 have large errors in both magnitude and direction. Lowering the threshold further increases
320 confidence, but at the expense of sample size. To effectively filter curlometry output, a more
321 complete analysis of tetrahedron and environmental parameters needs to be constructed, both
322 through higher-degree estimates of nonlinear magnetic field gradient and the orientation with
323 respect to the tetrahedron. Curlometer uncertainties stem not only from tetrahedron geometry, but
324 from the geometry in combination with the magnetic environment. Then, additional quality
325 standards can be developed to increase trustworthiness of current calculation at the expense of the
326 resolution.

327 **4.2. Single-Event Current Features**

328 Figure 4 provides a representative sample of a single perigee pass, from 10 October 2003.
329 This is the actual curlometer calculation from magnetometer observations, in contrast to the
330 simulation in Figure 3. While the observed current structures varied widely across the total dataset,
331 this event provides a typical case that shows common trends and avoids extremes. It is important
332 to note that the tetrahedron characteristic size varies greatly between data from 2001, 2002, and
333 2003-04 flight configurations. Thus, the example chosen in Figure 4 represents the most
334 observations but not necessarily the best. As in Figure 1, the spacecraft are traversing the inner
335 magnetosphere from the Southern Hemisphere to the Northern Hemisphere with only small
336 meridional deviation. The magnetic equator is crossed near 13:00 UTC, and this pass is located at

337 local time 09:40. Figure 4a shows curlometer output in SM Cartesian current components, with
338 the components clearly diverging later in the timeseries. The total current magnitude is plotted in
339 black. Figure 4b displays the azimuthal current component computed from the Cartesian
340 components. These current values are then compared to the quality parameter $Q = \text{div}(\mathbf{B})/\text{curl}(\mathbf{B})$
341 in Figure 4c and the tetrahedron geometry in the form of elongation (red) and planarity (blue) in
342 Figure 4d. Note that the geometrics are plotted on separate y-axes in Figure 4d to capture detail.
343 The plot limit times have been chosen to fully enclose spacecraft perigee by several hours and with
344 the “smooth” sections used as a means for identifying the region of interest.

345 For this inner-magnetospheric traversal, a few key features immediately stand out. The
346 Cartesian current components quickly diverge near the end of the selected data (Figure 4a), which
347 in turn causes the azimuthal current component to develop a strong negative trend (Figure 4b).
348 Figure 4b shows an environment where the azimuthal current is westward in the Southern
349 Hemisphere before decreasing to 0 just north of the magnetic equator and becoming eastward into
350 the Northern Hemisphere. This is clearly nonphysical behavior, and cannot be trusted to accurately
351 represent the ring current. Given the south-to-north trajectory, the azimuthal current should vary
352 with radial distance/L-shell, not with latitude as seen here. Instead, the curlometer-derived current
353 topology in Figure 4 looks very similar to the simulated environment in Figure 3, suggesting false
354 currents are to blame for the divergence. The large uncertainty in the data is corroborated by the
355 calculation of Q , which is only below the standard threshold of 0.5 in the beginning of the flight
356 track (Figure 4c). However, even during periods of relatively high confidence, the currents are still
357 diving towards negative values. A potential explanation for the diverging current lies in the
358 tetrahedron geometry (Figure 4d), which has a high elongation ($E > 0.8$) and an increasing
359 planarity (from $P < 0.4$ to $P = 1$) where low values are more regular and desirable. These extreme
360 geometric factors produce false currents as in Section 3.



362 In all orbits where Cluster achieved relatively regular tetrahedra when traversing the ring
363 current region, curlometry results varied greatly in structure and magnitude. Nearly all passes had
364 azimuthal current components in a westward direction with a magnitude peaking at or below 10
365 nA/m². Many perigee passes also featured similar azimuthal current profiles to the one on 10
366 October 2003 in Figure 4. This is inconsistent with our understanding of physical current structures
367 (e.g., Ganushkina et al., 2018), and calls the curlometer result for these diverging regions into
368 serious doubt. Data from 2003-2004 is especially susceptible to the decrease and reversal of
369 azimuthal current in similar fashion to Figure 4b, especially in regions where the tetrahedron
370 evolves to higher planarity. While the azimuthal current never becomes negative while $Q < 0.5$, it
371 does begin to decrease towards zero within this criterion.

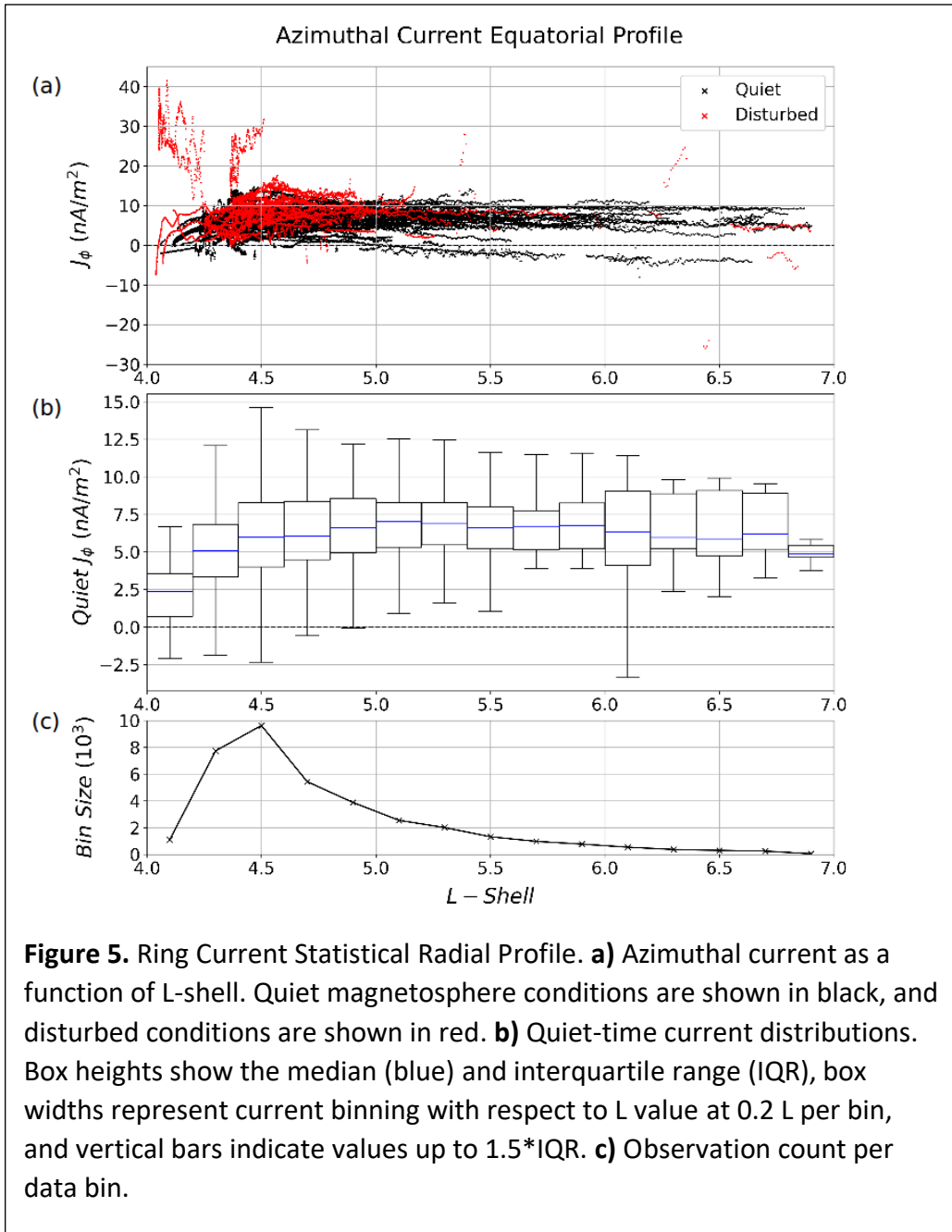
372 Curlometer output also showed large cross-hemisphere field-aligned currents (FACs),
373 around 10 nA/m² on 10 October 2003. This can be seen in Figure 4a using the J_z component as a
374 proxy for FACs due to magnetic field lines primarily along that axis. The persistence of FACs in
375 the curlometer output for all events will be discussed in more detail in the next section.

376 **4.2. Cluster-Derived Ring Current Environment**

377 If the simulated current environments and the false currents produced in those simulations
378 have any bearing on the actual ring current system, similar effects should appear in curlometer
379 output using the original spacecraft magnetic field observations. To establish a view of the ring
380 current at all local times, it is important to have a large and representative sample of measurements
381 throughout the whole precession of the Cluster orbit. This aim would be hindered by the extensive
382 data filtering required to produce meaningful curlometer results, removing any non-physical
383 results or using an advanced algorithm to determine magnetic gradient nonlinearity. Thus, the
384 holistic plots here are subject only to the restriction on quality parameter Q , and investigated for
385 signs of false current presence despite an accepted quality.

386 All perigee passes are considered in Figure 5. Taking data with $Q < 0.5$ and with $L < 7 R_E$,
387 events were sorted into “disturbed-time” and “quiet-time” categories delineated by $Dst = -25$ nT.
388 This threshold was set to have a very clear set of “quiet-time” observations, despite placing some
389 nearly-quiet observations into the “disturbed” category. Figure 5a provides curlometer output for
390 disturbed magnetospheric conditions (red data) and for quiet conditions (black data) as a function

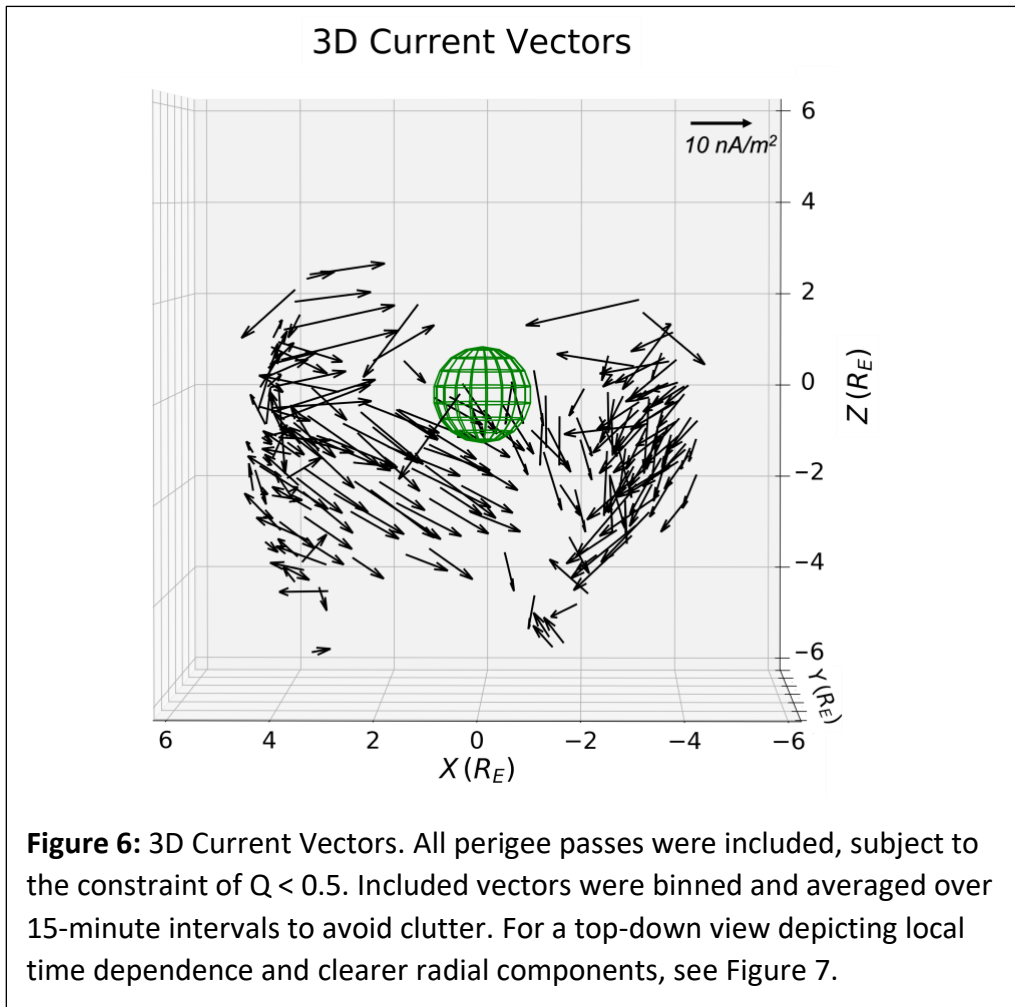
391 of L-shell. While disturbed events can show wild variation and sparse data coverage, quiet events
 392 provide insight into the radial ring current distribution. The spread of quiet data only is visualized
 393 via boxplot in Figure 5b, binned by L-shell in 0.2 R_E increments. Figure 5c shows the number of
 394 observed current values in each bin. The majority of ring current observations with $Q < 0.5$ lie
 395 Earthward of $L = 5$, so conclusions in this region are more robust.



397 The ring current as measured by Cluster between 2001 and 2004 was largely below 10
398 nA/m² in magnitude, with a marked decrease towards $L = 4 R_E$. This suggests that the eastward
399 reversal of the ring current usually lies inside the Cluster orbit and is not observed, although there
400 is less data in this region, and agrees with prior studies (Shen et al., 2014; Vallat et al., 2005).
401 However, at all values of L , the median of ring current magnitudes was below 7.5 nA/m², and the
402 third quartile was below 10 nA/m², as seen in Figure 5b. This better agrees with plasma pressure
403 calculations but contradicts earlier curlometry, such as the results of Vallat et al. (2005).
404 Additionally, this could still be impacted by up to 2 nA/m² of uncertainty from magnetometer
405 resolution, and by the production of false currents. For disturbed magnetospheric conditions, less
406 data were available and the scatterplot reveals higher spread (red data, Figure 5a). The linearization
407 assumption becomes even less robust during geomagnetic activity, because the extent of via viable
408 disturbed-time data is much smaller than quiet-time data (the limiting factor is usually that $Q < 0.5$
409 for a shorter duration). Nevertheless, the radial profiles of azimuthal current shown in Figure 5 do
410 not show any characteristic signs of contamination by false currents.

411 Figure 6 visualizes a subset of the full current vectors in 3D space. The data were subjected
412 to the same quality constraint $Q < 0.5$ as before and were then binned and averaged in 15-minute
413 intervals for plotting clarity. The plot contains both disturbed and quiet-time data, and all local
414 times. In this figure the J_z component is strong in most cases, and almost always negative. In fact,
415 the dominant current at most latitudes is southward field-aligned current as indicated by the arrows
416 generally pointing southward. The largest FACs are in excess of 20 nA/m² in perigee passes from
417 2002, and FACs in most other orbits were southward at ~ 5 nA/m² and did not vary significantly
418 between hemispheres. Prior curlometer analyses do not focus on FACs because they are
419 understood to be poorly represented. However, the topological identification of FACs has
420 precedent (e.g., Vallat et al., 2005, Zhang et al., 2011). This is the first report of such large currents
421 in such consistent direction, and should be viewed with extreme caution. The FACs in the inner
422 magnetosphere are not expected to be so persistently in the same cross-equatorial direction at all
423 latitudes and local times. Thus, the large field-aligned component provides evidence that the
424 curlometer output may not be a good representation of the actual currents. A consistent current of
425 this magnitude and direction is characteristic of false currents produced by the curlometer
426 technique under unfavorable magnetic environments. Because of the interconnected nature of
427 curlometer output components, these FACs also call the azimuthal currents computed by

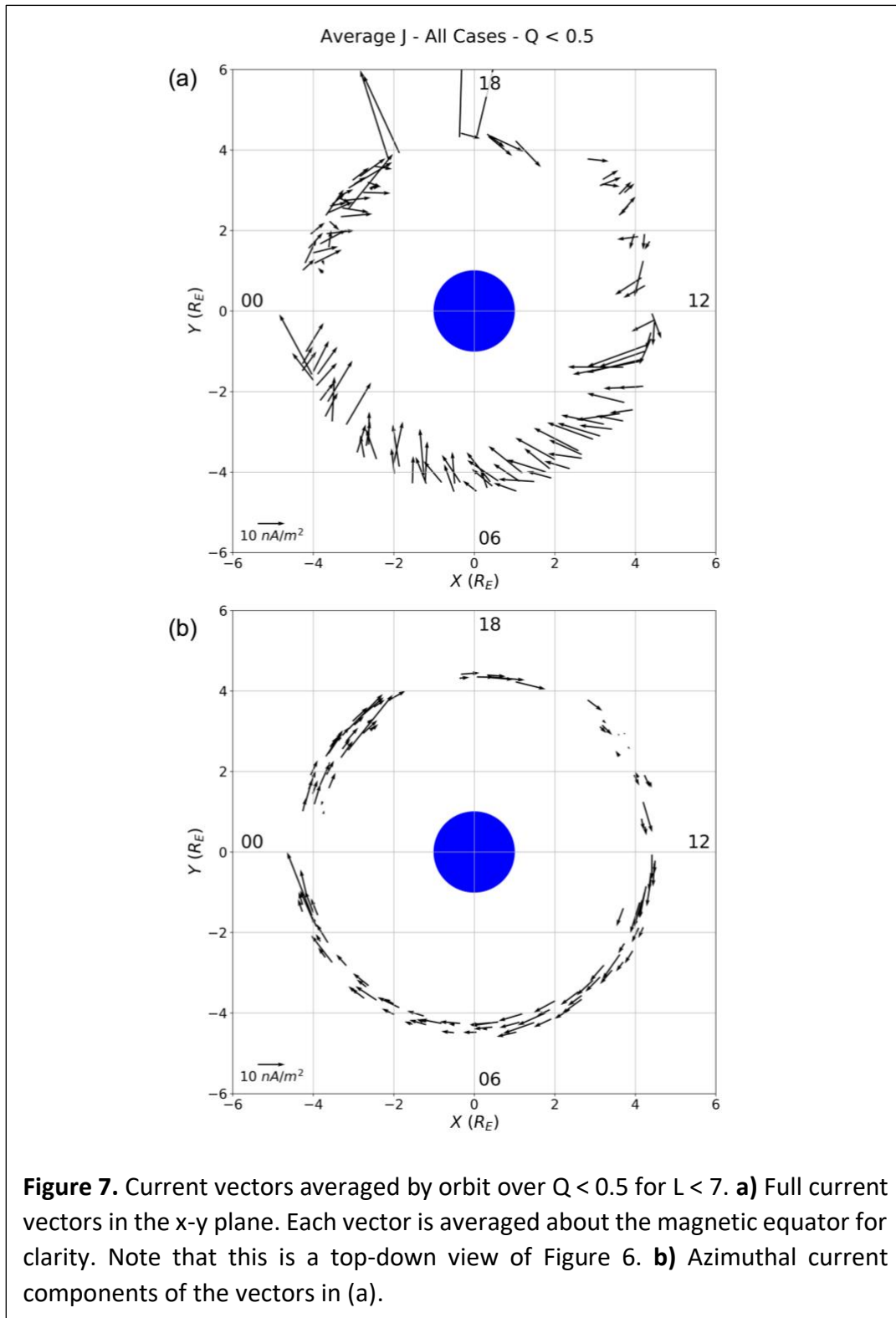
428 curlometry into question. This ubiquity and consistency of a southward FAC, regardless of
 429 geomagnetic activity, latitude, or local time, is characteristic of false currents.



430

431 For further visualization of these non-physical curlometer outputs, currents with $Q < 0.5$
 432 inside $L = 7$ (same criteria as Figure 5) were averaged for each perigee pass; the results are
 433 provided in Figure 7. Figure 7a shows the full horizontal current vectors, and Figure 7b shows just
 434 the azimuthal component. Note the large radial components of current at all local times for nearly
 435 all events in Figure 7a; this is not expected quiescent ring current structure (e.g., see review and
 436 references by Ganushkina et al., 2018), nor has it been reported in any previous study.
 437 Consideration of just the pure azimuthal component (Figure 7b) provides a misleading picture
 438 because it omits the strong Earthward components, as well as the z-component as seen in Figure
 439 6. Providing the full current vector or combining azimuthal and radial components adds additional

440 evidence of the presence of false currents by allowing the full complexity of the output currents
 441 that lack a plausible physical explanation.



443 While the above estimates provide methodically-consistent ring current computation, each
444 perigee pass can also be assessed individually to account for signs of nonphysical output in the
445 computed currents. These include the divergent current components as displayed in Figure 4a.
446 Data from 2001 should be discarded because it does not usually show a clear transition to the ring
447 current region, and because the tetrahedron characteristic size is larger than 1000 km. Additionally,
448 data from the 2003-2004 orbits can sometimes be noisy or have large cross-equatorial trends that
449 should be eliminated. Finally, the case from 18 March 2002 should be excluded from holistic
450 analysis because of the uniqueness of the observed current structure. Despite the focus on this
451 event in Vallat et al. (2005), the physical implications for plasma populations and magnetic
452 topology necessitated by a constant and strong ring current through a large swath of the orbit
453 require special case study. However, aggressive removal of non-ideal perigee passes does not alter
454 the persistent large FACs show in Figure 6 and Figure 7, nor the radial profile in Figure 5. This
455 suggests a systematic presence of curlometer errors that are appearing in all cases, regardless of
456 the available filtering criteria.

457 Considering these structures and the likely reasons for the non-physical currents, Cluster
458 curlometer output is limited for assessing the inner magnetospheric ring current density. There is
459 more information contained in analysis of individual passes than in views of the system as a whole,
460 and qualitative trends provide the most confidence in these cases. It is sufficient to note that the
461 ring current is a highly-variable structure, in both magnitude and extent, and therefore small
462 variations in the environment can lead to drastic changes. Without a definitive way to remove the
463 full 3D effects of false current generation, however, quantitative analysis of ring current Cluster
464 data has significant uncertainty that precludes definitive determination of current densities and
465 orientations.

466 **5. Discussion**

467 The curlometer technique has produced unexpected results in the discussed applications:
468 simulated current environments, single perigee passes, and holistic studies of all available events.
469 In the simulated current environments, the curlometer calculation reproduced the imposed current
470 with high fidelity in regular tetrahedra. The best results occur where nonlinearities were
471 constrained or eliminated (Dunlop et al., 2020). However, using actual spacecraft position data

472 and a nonlinear magnetic environment, false currents were detected by the curlometer that were
473 not imposed in the simulation. These false currents were produced while the quality parameter Q
474 was within standard thresholds. Standing alone, this directly challenges the efficacy of Q but does
475 not imply anything about the ring current itself. However, single perigee passes also displayed
476 unique current structures. The strong hemispheric asymmetry of the current throughout the perigee
477 passes, especially in the 2003 data where current components remained continuous without sudden
478 spikes but diverged later in the flight track, casts doubt on the validity of the observed structure.
479 These structures are contrary to plasma organization by magnetic field lines, which are oriented
480 cross-hemisphere, and disagree with a pressure peak at low latitude. Although much of the
481 divergent current region lies outside of $Q < 0.5$ and is therefore untrustworthy, the trends begin
482 well within the filtered data. The diverging currents increase with tetrahedron irregularity,
483 suggesting a causal relationship. In light of the simulated false currents, which also produce this
484 divergence with tetrahedron irregularity, the single perigee passes all seem to contain some
485 combination of poor tetrahedron quality or strong magnetic gradient that produces poor current
486 estimates.

487 Radial and 3D plots of full current vectors combined from all perigee passes analyzed by
488 curlometry are similarly unexpected. Currents are dominated by a large field-aligned component
489 in both hemispheres at all local times that is southward and cross-equatorial. There is also a
490 significant radial component Earthward at all local times. The most valuable product is azimuthal
491 current as a function of L-shell, which produces a consistent value for quiet-time ring current below
492 10 nA/m^2 and hints at a current reversal to the eastward ring current within $L = 4$. Although less
493 steep than anticipated, the curlometer does detect a radial current peak. Attempts to clarify and
494 sharpen these analyses by restricting data to stable, trustworthy, or expected structure for
495 individual perigee passes using established quality indices were unsuccessful in refining the
496 dataset. Therefore, the ring current using Cluster data must stand as presented here, including the
497 unusual features and limitations, and the confounding presence of false currents that greatly
498 increase uncertainty.

499 Revisitation of Cluster ring current computation has called into question the efficacy of the
500 curlometer technique in this region due to increased uncertainty. Individual time series plots show
501 clear errors in current magnitude and direction, especially when the tetrahedron is distorted.

502 Furthermore, extensive simulation shows that the parameter Q does not always accurately
503 represent the current estimate quality, and at the accepted threshold of $Q < 0.5$ can produce false
504 currents as large as 100% of the actual current in complementary components. Lowering the
505 threshold reduces the sample size to a highly-restricted domain that obscures sought trends.
506 Previous current estimates of ~ 20 nA/m² are nevertheless not upheld by this study, with quiet cases
507 overwhelmingly below 10 nA/m².

508 The discrepancy between legacy plasma moment estimates of ring current strength and
509 distribution and Cluster curlometer values has narrowed significantly, with a newfound magnitude
510 median peaking at just 7 nA/m². The new analysis presented above finds that the ring current is
511 weaker during the 2002-2004 period than some previous curlometer estimates. Climatologies
512 using these data should nevertheless be extremely cautious of the quality of current estimates, and
513 effectively removing unsatisfactory cases reduces the sample size to preclude judgment on large-
514 scale trends without removing the effects of false currents.

515 **6. Conclusions**

516 This study conducted a systematic assessment of current calculations using the curlometry
517 technique in the inner magnetosphere, using the specific satellite alignments of the Cluster mission
518 when it had a tetrahedral configuration at perigee. It was found that curlometry sometimes yields
519 excellent reproductions of imposed currents, but other times produces large false currents due to
520 the linearization within the calculation. The appearance of false currents is directly related to the
521 orientation of the tetrahedron relative to the imposed current. Specifically, it was determined that
522 larger false currents are produced when the largest planar semiaxis of the tetrahedron is more
523 parallel to the local gradient of the magnetic field. These false currents can appear even when the
524 elongation and planarity parameters signify only limited tetrahedron irregularity, and can be quite
525 large even when the Q factor is below the nominally acceptable level of 0.5.

526 Keeping these limitations in mind, a statistical compilation of inner magnetospheric
527 currents was then calculated. Although the new median ring current density of 7 nA/m² is in better
528 agreement with other computation methods, there are still uncertainties associated with this
529 measurement. The instrument magnetic field resolution alone introduces ± 1.5 nA/m² of
530 uncertainty (Vallat et al., 2005), and one must also consider the presence of false currents as an
531 artifact of the nonlinearity. Even at $Q < 0.5$, these uncertainties can be quite large or even dominate

532 the observed current structure, and are difficult to remove because of the complex dependence on
533 tetrahedron orientation relative to the unknown currents. Furthermore, the interdependent nature
534 of the curlometer current components necessitates the consideration of the large radial and field-
535 aligned currents, which raise additional concerns due to unexpected structure.

536 Thus, any inner magnetospheric curlometry analysis that relies on Cluster ring current data,
537 including magnitudes and climatologies, should be viewed with full knowledge of the caveats and
538 limitations described herein. Although shortcomings in curlometry are discussed in detail here, the
539 extent of this analysis is restricted to Cluster spacecraft within the specified orbits and around
540 perigee. The use of curlometry elsewhere should be examined for similar effects, but the
541 uncertainties in the ring current region cannot be directly applied to other regions because of the
542 strong dependence on magnetic field nonlinearity and tetrahedron shape/orientation.

543 **Acknowledgments and Data**

544 This project was funded in part through a grant from the National Science Foundation's
545 Research Experience for Undergraduates Program (Grant Number 1659248) and NSF grant
546 1663770, as well as by NASA grants 80NSSC17K0015 and NNX17AB87G. The authors give
547 special thanks to the developers and curators of the SpacePy Python package, which proved
548 invaluable for coordinate conversions and data processing. We would also like to acknowledge Dr.
549 Michael Hirsch for use of his Python igrf12 package. DOI: 10.5281/zenodo.3461075. Cluster
550 magnetometer data used in this study are available at the Cluster Science Archive
551 (<https://csa.esac.esa.int/csa-web/>) and at NASA/GSFC's Space Physics Data Facility's CDAWeb
552 service (<https://cdaweb.gsfc.nasa.gov/>), accessed October 2018. The simulated data sets and
553 Python code are available at the University of Michigan Deep Blue data repository
554 (<https://deepblue.lib.umich.edu/data>). We will "mint a DOI" to finalize and freeze the data brick
555 upon acceptance.

556

557 **References**

558 Alken, P., Thébaud, E., Beggan, C. D., Amit, H., Aubert, J., Baerenzung, J., et al. (2021).
559 International Geomagnetic Reference Field: the thirteenth generation. *Earth, Planets and*
560 *Space*, 73, 49. <https://doi.org/10.1186/s40623-020-01288-x>

- 561 Balogh, A., Dunlop, M. W., Cowley, S. W. H., Southwood, D. J., Thomlinson, J. G., Glassmeier,
562 K. H., et al. (1997). The Cluster Magnetic Field Investigation. *Space Science Reviews*,
563 79, 65–91. <https://doi.org/10.1023/A:1004970907748>
- 564 Balogh, A., Carr, C. M., Acuña, M. H., Dunlop, M. W., Beek, T. J., Brown, P., et al. (2001). The
565 Cluster Magnetic Field Investigation: overview of in-flight performance and initial
566 results. *Annales Geophysicae*, 19(10/12), 1207–1217. [https://doi.org/10.5194/angeo-19-](https://doi.org/10.5194/angeo-19-1207-2001)
567 1207-2001.
- 568 Daly, P. W., & Kronberg, E. A. (2013). User Guide to the RAPID Measurements in the Cluster
569 Science Archive (CSA) (5.4). Goettingen, Germany.
- 570 Dandouras, I., & Barthe, A. (2011). User Guide to the CIS measurements in the Cluster Active
571 Archive (CAA) (Vol. 2.0).
- 572 Dandouras, I., & Barthe, A. (2015). Cluster Active Archive: Interface Control Document for
573 CIS.
- 574 Dandouras, I., Rochel-Grimald, S., Vallat, C., & Dunlop, M. W. (2018). Terrestrial ring current:
575 A review of Cluster results based on the curlometer technique. *Electric Currents in*
576 *Geospace and Beyond*. <https://doi.org/10.1002/9781119324522.ch7>.
- 577 Dunlop, M. W., Balogh, A., Glassmeier, K.-H., & Robert, P. (2002). Four-point Cluster
578 application of magnetic field analysis tools: The Curlometer. *Journal of Geophysical*
579 *Research*, 107, 1384. DOI:10.1029/2001JA005088.
- 580 Dunlop, M. W., Haaland, S., Dong, X. C., Middleton, H. R., Escoubet, C. P., Yang, Y. Y., et al.
581 (2018). Multipoint analysis of electric currents in geospace using the curlometer
582 technique. *Electric Currents in Geospace and Beyond*, 67–80.
583 <https://doi.org/10.1002/9781119324522.ch4>.
- 584 Dunlop, M. W., Haaland, S., Escoubet, P. C., & Dong, X.-C. (2016). Commentary on accessing
585 3-D currents in space: Experiences from Cluster. *Journal of Geophysical Research:*
586 *Space Physics*, 121(8), 7881–7886. <https://doi.org/10.1002/2016JA022668>.
- 587 Dunlop, M. W., Southwood, D. J., Glassmeier, K. H., & Neubauer, F. M. (1988). Analysis of
588 multipoint magnetometer data. *Advances in Space Research*, 8(9–10), 273–277.
589 [https://doi.org/10.1016/0273-1177\(88\)90141-X](https://doi.org/10.1016/0273-1177(88)90141-X).

- 590 Dunlop M.W., Yang J.Y., Yang Y.Y., Lühr H., Cao J.B. (2020). Multi-spacecraft Current
591 Estimates at Swarm. In: Dunlop M., Lühr H. (eds) Ionospheric Multi-Spacecraft Analysis
592 Tools. ISSI Scientific Report Series, vol 17. Springer, Cham. [https://doi.org/10.1007/978-](https://doi.org/10.1007/978-3-030-26732-2_5)
593 [3-030-26732-2_5](https://doi.org/10.1007/978-3-030-26732-2_5)
- 594 Dunlop, M. W., Yang, J. Y., Yang, Y. Y., Xiong, C., Lühr, H., Bogdanova, Y. V., et. al (2015).
595 Simultaneous field-aligned currents at Swarm and Cluster satellites. *Geophysical*
596 *Research Letters*, 42(10), 3683–3691. <https://doi.org/10.1002/2015GL063738>.
- 597 Fränz, M., & Harper, D. (2002). Heliospheric coordinate systems. *Planetary and Space Science*,
598 50(2), 217–233. [https://doi.org/10.1016/S0032-0633\(01\)00119-2](https://doi.org/10.1016/S0032-0633(01)00119-2).
- 599 Ganushkina, N. Y., Liemohn, M. W., Dubyagin, S., Daglis, I. A., Dandouras, I., DeZeeuw, D. L.,
600 et. al (2015). Defining and resolving current systems in geospace. *Annales Geophysicae*,
601 33, 1269-1402. doi:10.5194/angeo-33-1369-2015
- 602 Ganushkina, N. Y., Liemohn, M. W., & Dubyagin, S. (2018), Current systems in the Earth's
603 magnetosphere, *Reviews of Geophysics*, 56(2), 309-332, doi: 10.1002/2017RG000590.
- 604 Greenspan, M. E., & Hamilton, D. C. (2000). A test of the Dessler-Parker-Sckopke relation
605 during magnetic storms. *Journal of Geophysical Research Space Physics*, 105, 5419-
606 5430.
- 607 Grimald, S., Dandouras, I., Robert, P., & Lucek, E. (2012). Study of the applicability of the
608 curlometer technique with the four Cluster spacecraft in regions close to Earth. *Annales*
609 *Geophysicae*, 30(3), 597–611. <https://doi.org/10.5194/angeo-30-597-2012>.
- 610 Hapgood, M. A. (1992). Space physics coordinate transformations: A user guide. *Planetary and*
611 *Space Science*, 40(5), 711–717. [https://doi.org/10.1016/0032-0633\(92\)90012-D](https://doi.org/10.1016/0032-0633(92)90012-D).
- 612 Henderson, P. D., Owen, C. J., Lahiff, A. D., Alexeev, I. V., Fazakerley, A. N., Yin, L., et al.
613 (2008). The relationship between $\mathbf{j} \times \mathbf{B}$ and $\nabla \cdot \mathbf{P}_e$ in the magnetotail plasma sheet: Cluster
614 observations. *Journal of Geophysical Research: Space Physics*, 113(7), 1–17.
615 <https://doi.org/10.1029/2007JA012697>.

- 616 Laakso, H., Perry, C., McCaffrey, S., Herment, D., Allen, A. J., Harvey, C. C., et al. (2010).
617 Cluster Active Archive: Overview. In H. Laakso et al. (Ed.), *Astrophysics and Space*
618 *Science Proceedings* (pp. 3–37).
- 619 Le, G., Russell, C. T., & Takahashi, K. (2004). Morphology of the ring current derived from
620 magnetic field observations. *Annales Geophysicae*, 22, 1267-1295. 10.5194/angeo-22-
621 1267-2004.
- 622 Liemohn, M. W., Kozyra, J. U., Thomsen, M. F., Roeder, J. L., Lu, G., Borovsky, J. E., &
623 Cayton, T. E. (2001). Dominant role of the asymmetric ring current in producing the
624 stormtime Dst*, *Journal of Geophysical Research*, 106, 10883-10904.
625 DOI:10.1029/2000JA000326.
- 626 Liemohn, M. W., Kozyra, J. U., Clauer, C. R., & Ridley, A. J. (2001). Computational analysis of
627 the near-Earth magnetospheric current system, *Journal of Geophysical Research*, 106,
628 29,531, 2001. DOI: 10.1029/2001JA000045.
- 629 Liemohn, M. W., Katus, R. M., & Ilie, R. (2015), Statistical analysis of storm-time near-Earth
630 current systems, *Annales Geophysicae*, 33, 965-982, doi: 10.5194/angeo-33-965-2015.
- 631 Liemohn, M. W., Ganushkina, N. Y., Ilie, R., & Welling, D. T. (2016). Challenges associated
632 with near-Earth nightside current. *Journal of Geophysical Research: Space Physics*, 121,
633 6763–6768. <https://doi.org/10.1002/2016JA022948>.
- 634 Lui, A. T. Y., & Hamilton, D. C. (1992). Radial profiles of quiet time magnetospheric
635 parameters. *Journal of Geophysical Research*, 97(A12), 19325.
636 <https://doi.org/10.1029/92ja01539>.
- 637 Lui, A. T. Y., McEntire, R.W., & Krimigis, S. M. (1987). Evolution of the ring current during
638 two geomagnetic storms. *Journal of Geophysical Research*, 92, 7459–7470.
- 639 Middleton, H., & Masson, A. (2016). The Curlometer technique: a beginner’s guide. ESDC-
640 CSA-TN-0001 (Vol. 1).
- 641 Milillo, A., Orsini, S., & Daglis, I. A. (2001). Empirical model of proton fluxes in the equatorial
642 inner magnetosphere: Development. *Journal of Geophysical Research Space Physics*,
643 106, 25,713-25,729.

- 644 Milillo, A., Orsini, S., Delacourt, D. C., Mura, A., Massetti, S., De Angelis, E., & Ebihara, Y.
645 (2003), Empirical model of proton fluxes in the equatorial inner magnetosphere: 2.
646 Properties and applications, *Journal of Geophysical Research Space Physics*, 108, A5.
647 1165// <https://doi.org/10.1029/2002JA009581>
- 648 Morley, S., Koller, J., Welling, D., Larsen, B., Henderson, M., & Niehof, J. (2011). “Spacepy - A
649 Python-based library of tools for the space sciences”. In “*Proceedings of the 9th Python
650 in science conference (SciPy 2010)*”.
- 651 Paschmann, G., & Daly, P. W. (2000). Analysis Methods for Multi-Spacecraft Data. ISSI
652 Scientific Report.
- 653 Petrukovich, A., Artemyev, A., Vasko, I., Nakamura, R., & Zelenyi, L. (2015). Current Sheets in
654 the Earth Magnetotail: Plasma and Magnetic Field Structure with Cluster Project
655 Observations. *Space Science Reviews*, 188(1–4), 311–337.
656 <https://doi.org/10.1007/s11214-014-0126-7>.
- 657 Reme, H., Bosqued, J. M., Sauvaud, J. A., Cros, A., Dandouras, J., Aoustin, C., et al. (1997). The
658 Cluster Ion Spectrometry (CIS) Experiment. *Space Science Reviews*, 79, 303–350.
659 Retrieved from http://www.space.irfu.se/exjobb/2003_erik_bergman/articles/CIS.pdf
- 660 Robert, P., Dunlop, M. W., Roux, A., & Chanteur, G. (1998). Reprinted from Analysis Methods
661 for Multi-Spacecraft Data Accuracy of Current Density Determination 16.1 Introduction.
662 In G. Paschmann & P. W. Daly (Eds.), *Analysis Methods for Multi-Spacecraft Data* (1.1,
663 pp. 395–418). ISSI/ESA.
- 664 Sergis, N., Krimigis, S. M., Mitchell, D. G., Hamilton, D. C., Krupp, N., Mauk, B. M., et al.
665 (2007). Ring current at Saturn: Energetic particle pressure in Saturn’s equatorial
666 magnetosphere measured with Cassini/MIMI. *Geophysical Research Letters*, 34(9), 1–6.
667 <https://doi.org/10.1029/2006GL029223>.
- 668 Shen, C., Yang, Y. Y., Rong, Z. J., Li, X., Dunlop, M., Carr, C. M., et al. (2014). Direct
669 calculation of the ring current distribution and magnetic structure seen by Cluster during
670 geomagnetic storms. *Journal of Geophysical Research: Space Physics*, 119(4), 2458–
671 2465. <https://doi.org/10.1002/2013JA019460>.

672 Vallat, C., Dandouras, I., Dunlop, M., Balogh, A., Lucek, E., Parks, G. K., et al. (2005). First
673 current density measurements in the ring current region using simultaneous multi-
674 spacecraft CLUSTER-FGM data. *Annales Geophysicae*, 23(5), 1849–1865.
675 <https://doi.org/10.5194/angeo-23-1849-2005>.

676 Zhang, Q. H., Dunlop, M. W., Lockwood, M., Holme, R., Kamide, Y., Baumjohann, W., et al.
677 (2011). The distribution of the ring current: Cluster observations. *Annales Geophysicae*,
678 29(9), 1655–1662. <https://doi.org/10.5194/angeo-29-1655-2011>.

679